Simulation of Open- and Ducted-Rotor Noise Using CAA-Multidomain Method

Jianping Yin, Jan W. Delfs
DLR, Institut fuer Aerodynamik und Stroemungstechnik, Technische Akustik
Lilienthalplatz 7, 38108 Braunschweig, Germany
e-mail: Jianping.yin@dlr.de

Abstract

The sound field generated by an open rotor and that radiated by the same rotor placed inside a semi-infinite duct is simulated using a Computational Aeroacoustic (CAA) multi-domain method. The linearized Euler equations in cylindrical coordinates are used as governing equations in solving this problem. Both Tam's radiation and PML boundary conditions are used. Comparisons of results by using the two different far-field boundary conditions will be given. A multi-domain Cartesian grid system is used so that the number of grid points can be kept as a minimum. A combination of DRP and a specially optimized cell-centered high order differencing scheme is implemented in the area of two Cartesian grid interfaces. The effect of mean flow including a shear layer on the noise radiation off the ducted rotor is studied.

1. Introduction

The prediction of open or ducted rotor noise as shown in Fig.(1) is a challenging problem as there are large difference in scales between the noise source near the rotor and the sound field. The most commonly used methods for this type of problem are integral methods based on both FW-H and Kirchhoff formulations[1,2]. These approaches to compute noise radiation from rotors in the subsonic flow regime are split into two steps. In a first step, the near-field aerodynamics and acoustics close to the source, or on the surface when using FW-H with impenetrable surface, are computed using an aerodynamics code. This then serves as input to the integral method which computes the acoustic pressure at any desired observer location in the far-field. For the computation of acoustic propagation over large distances without dissipation, these hybrid methods are much more computationally efficient than CFD methods, but they suffer from the limitation that acoustic waves are assumed to propagate through a medium which is largely at rest or at most in uniform motion relatively to the observer.

In the present paper, the sound field generated by an open and ducted rotor is simulated using Computational Aeroacoustics (CAA). The CAA method [3] has the advantage over a CFD method in accurately predicting small amplitude acoustic fluctuations and their correct propagation to the far field even in non-uniform flow. The linearized Euler Equations (LEE) are used as governing equations in solving this problem. The problems considered are taken from the third CAA benchmark problems workshop[4]. In this benchmark problem, a rotor is simplified as distribution of a rotating force acting on the fluid. In the far-field area of the computation domain as well as the duct inflow in the ducted rotor case, both Tam's radiation and Perfect Matched Layer (PML)[5] boundary conditions are used. Comparisons of results by using the two different far-field boundary conditions will be given. Because of the disparity between the length scales in the source region and the acoustic wavelengths, a multi-domain Cartesian grid system is used in which local resolution enhancement is achieved by stepping the grid size of neighboring Cartesian grid blocks by factors of two so that the number of grid points can be kept as a minimum. In the area of two Cartesian grid interfaces, a combination of Tam & Webb's DRP and a specially optimized cell-centered high order differencing scheme is implemented [6,7].

The report is structured as follows. The governing equations, numerical schemes, boundary conditions and multi-domain method are discussed at first. The noise radiation from open and ducted rotor with subsonic and supersonic rotational speeds are studied. Some of the results are compared with the

Paper presented at the RTO AVT Symposium on "Ageing Mechanisms and Control: Part A – Developments in Computational Aero- and Hydro-Acoustics", held in Manchester, UK, 8-11 October 2001, and published in RTO-MP-079(I).

analytical solutions. In order to demonstrate the effect of mean flow on the noise radiation off the ducted rotor, a mean flow is introduced including a shear layer, separating the ambient medium from the jet flow exiting out of the duct.

2. Governing Equations

The basic set of equations for the present analysis are the three dimensional LEE with a non-uniform mean flow in cylindrical coordinates. Under the assumption that the perturbations are small, LEE can be obtained by splitting the flow variables of the Euler equations into the mean and perturbation terms. The linear perturbation field represents acoustic, vorticity and entropy waves. The linearized perturbation equations or LEE about the mean flow in cylindrical coordinates then have the following forms :

$$
\begin{aligned}
&\frac{\partial \rho'}{\partial t}+\bar{u}\frac{\partial \rho'}{\partial x}+\bar{v}\frac{\partial \rho'}{\partial r}+\frac{\bar{w}}{r}\frac{\partial \rho'}{\partial \theta}+\bar{\rho}\left(\frac{\partial u'}{\partial x}+\frac{\partial v'}{\partial r}+\frac{\partial w'}{r\partial \theta}+\frac{v'}{r}\right)+\frac{\rho'\bar{v}}{r}= \\
&\qquad -\bar{u}_x\rho'-\bar{\rho}_x u'-\bar{u}_r\rho'-\bar{\rho}_r v'-\bar{w}_\theta\frac{\rho'}{r}-\bar{\rho}_\theta\frac{w'}{r} \\
&\frac{\partial u'}{\partial t}+\bar{u}\frac{\partial u'}{\partial x}+\bar{v}\frac{\partial u'}{\partial r}+\frac{\bar{w}}{r}\frac{\partial u'}{\partial \theta}+\frac{1}{\bar{\rho}}\frac{\partial p'}{\partial x}=-\bar{u}_x u'-\bar{u}_r v'-\bar{u}_\theta\frac{w'}{r}+\frac{\bar{p}_x}{\bar{\rho}^2}\rho'+F_x(x,r,\theta) \\
&\frac{\partial v'}{\partial t}+\bar{u}\frac{\partial v'}{\partial x}+\bar{v}\frac{\partial v'}{\partial r}+\frac{\bar{w}}{r}\frac{\partial v'}{\partial \theta}-\frac{2\bar{w}w'}{r}+\frac{1}{\bar{\rho}}\frac{\partial p'}{\partial r}= \\
&\qquad -\bar{v}_x u'-\bar{v}_r v'-\bar{v}_\theta\frac{w'}{r}+\frac{\bar{p}_r}{\bar{\rho}^2}\rho'+F_r(x,r,\theta) \\
&\frac{\partial w'}{\partial t}+\bar{u}\frac{\partial w'}{\partial x}+\bar{v}\frac{\partial w'}{\partial r}+\frac{\bar{w}}{r}\frac{\partial w'}{\partial \theta}+\frac{(\bar{w}v'+\bar{v}w')}{r}+\frac{1}{\bar{\rho}r}\frac{\partial p'}{\partial \theta}= \\
&\qquad -\bar{w}_x u'-\bar{w}_r v'-\bar{w}_\theta\frac{w'}{r}+\frac{\bar{p}_\theta}{\bar{\rho}^2 r}\rho'+F_\theta(x,r,\theta) \\
&\frac{\partial p'}{\partial t}+\bar{u}\frac{\partial p'}{\partial x}+\bar{v}\frac{\partial p'}{\partial r}+\frac{\bar{w}}{r}\frac{\partial p'}{\partial \theta}+\frac{\gamma}{r}(\bar{p}v'+\bar{v}p')+\gamma\bar{p}\left(\frac{\partial u'}{\partial x}+\frac{\partial v'}{\partial r}+\frac{1}{r}\frac{\partial w'}{\partial \theta}\right)= \\
&\qquad -\bar{p}_x u'-\bar{p}_r v'-\bar{p}_\theta\frac{w'}{r}-\gamma\left(\bar{u}_x+\bar{v}_r+\frac{\bar{w}_\theta}{r}\right)p'
\end{aligned}
\tag{1}
$$

In which u', v' and w' are the axial (x), radial (r) and azimuth (θ) velocity perturbation components respectively. ρ' and p' are the density and the pressure respectively. $\bar{u}$, $\bar{v}$, $\bar{w}$, $\bar{p}$ and $\bar{\rho}$ are the corresponding mean values, and the subscripts x, r and θ denote their partial derivatives. The (F_x, F_r, F_θ) denote the components of the source term. All quantities are written in non-dimensionalized form with respect to length scale b (radius of the blade), velocity scale c (sound speed), time scale b/c, density scale ρ_0 (ambient density), and pressure scale $\rho_0 c^2$.

When a parallel mean flow condition ($\bar{u}\neq 0$, $\bar{v}=\bar{w}=0$ and $\bar{\rho}=\bar{p}=1$) is introduced, the Eq.(1) can be simplified as

$$
\begin{aligned}
&\frac{\partial u'}{\partial t}+\bar{u}\frac{\partial u'}{\partial x}+\frac{\partial p'}{\partial x}=-\bar{u}_r v'+F_x(x,r,\theta) \\
&\frac{\partial v'}{\partial t}+\bar{u}\frac{\partial v'}{\partial x}+\frac{\partial p'}{\partial r}=F_r(x,r,\theta) \\
&\frac{\partial w'}{\partial t}+\bar{u}\frac{\partial w'}{\partial x}+\frac{1}{r}\frac{\partial p'}{\partial \theta}=F_\theta(x,r,\theta) \\
&\frac{\partial p'}{\partial t}+\bar{u}\frac{\partial p'}{\partial x}+\frac{v'}{r}+\left(\frac{\partial u'}{\partial x}+\frac{\partial v'}{\partial r}+\frac{1}{r}\frac{\partial w'}{\partial \theta}\right)=0
\end{aligned}
\tag{2}
$$

Since for the parallel mean flow there is no coupling of the velocity and pressure perturbation with the density, the density equation contained in Eq.(1) is neglected in Eq.(2).

To simplify the problems while keeping the main physics, the rotor is replaced by a distribution of rotating body forces. The components of body force or the source terms (F_x, F_r, F_θ) in Eq.(1) and Eq.(2) are given from the third CAA benchmark problems workshop as follows,

$$\begin{bmatrix} F_x(x,r,\theta,t) \\ F_r(x,r,\theta,t) \\ F_\theta(x,r,\theta,t) \end{bmatrix} = \mathrm{Re}\left\{ \begin{bmatrix} \tilde{F}_x(x,r) \\ 0 \\ \tilde{F}_\theta(x,r) \end{bmatrix} e^{im(\theta-\Omega t)} \right\} \tag{3}$$

where Re{ }is the real part and ($\tilde{F}_x, \tilde{F}_\theta$) denotes the body force distribution in r and x. In addition, the m is the number of rotor blades and Ω is the angular velocity of the rotor. Therefore, the frequency of the radiated sound is $m\Omega$.

The actual rotor noise is a 3-D problem, but by factoring out the azimuthal dependence with

$$\begin{bmatrix} u'(x,r,\theta,t) \\ \mathrm{v}'(x,r,\theta,t) \\ \mathrm{w}'(x,r,\theta,t) \\ p'(x,r,\theta,t) \end{bmatrix} = \mathrm{Re}\left\{ \begin{bmatrix} \tilde{u}(x,r,t) \\ \tilde{\mathrm{v}}(x,r,t) \\ \tilde{\mathrm{w}}(x,r,t) \\ \tilde{p}(x,r,t) \end{bmatrix} e^{im\theta} \right\} \tag{4}$$

the problem can be reduced to a 2-D problem. Then the governing equations for ($\tilde{u}, \tilde{\mathrm{v}}, \tilde{\mathrm{w}}, \tilde{p}$) can be obtained by inserting Eq.(3) and Eq.(4) into Eq.(2),

$$\begin{aligned} &\frac{\partial \tilde{u}}{\partial t} + \bar{u}\frac{\partial \tilde{u}}{\partial x} + \frac{\partial \tilde{p}}{\partial x} = -\bar{u}_r \tilde{\mathrm{v}} + \tilde{F}_x(x,r)e^{-im\Omega t} \\ &\frac{\partial \tilde{\mathrm{v}}}{\partial t} + \bar{u}\frac{\partial \tilde{\mathrm{v}}}{\partial x} + \frac{\partial \tilde{p}}{\partial r} = 0 \\ &\frac{\partial \tilde{\mathrm{w}}}{\partial t} + \bar{u}\frac{\partial \tilde{\mathrm{w}}}{\partial x} + \frac{im}{r}\tilde{p} = \tilde{F}_\theta(x,r)e^{-im\Omega t} \\ &\frac{\partial \tilde{p}}{\partial t} + \bar{u}\frac{\partial \tilde{p}}{\partial x} + \frac{\tilde{\mathrm{v}}}{r} + \left(\frac{\partial \tilde{u}}{\partial x} + \frac{\partial \tilde{\mathrm{v}}}{\partial r} + \frac{im}{r}\tilde{\mathrm{w}}\right) = 0 \end{aligned} \tag{5}$$

The Eq.(5) will be used to solve open and ducted rotor problems. The solutions to the Eq.(5) can be directly discretized in x and r for Cartesian grids and a given parallel mean flow. The DRP finite difference scheme[8] and the artificial selective damping [9] are used for the spatial discretization.

2. Boundary Conditions

Due to the limitation of a finite computational domain, numerical outer boundary conditions are needed for the acoustic simulation. At the outer boundary of the computational domain, two types of non-reflecting boundary conditions are implemented. These are asymptotic radiation and outflow boundary conditions as well as PML[5] conditions. The details of the radiation and outflow boundary conditions developed by Tam and Dong were given in ref.[10]. In the case of ducted rotor, the solid wall boundary condition must be satisfied at the surface of the duct wall. In addition, along the axis of the cylindrical coordinates; i.e., $r = 0$, a special set of equations are used.

2.1 PML Boundary Conditions

The asymptotic radiation and outflow boundary conditions developed in ref.[10] can only be used for weakly non-uniform flow. Its use for the flow with strong shear layer across the far-field boundary area is not suitable. PML conditions are implemented as an absorbing boundary condition. One advantage of using PML is that PML can be easily implemented for non-uniform mean flow. The PML technique has proved to be effective and easy to implement. For the open and ducted rotor problems, the PML equations used in the PML domain are derived by splitting the variables of the governing equations (5) :

$$
\begin{aligned}
&\frac{\partial \tilde{u}_1}{\partial t}+\sigma_x \tilde{u}_1=-\bar{u}\frac{\partial \tilde{u}}{\partial x}-\frac{\partial \tilde{p}}{\partial x}\\
&\frac{\partial \tilde{u}_2}{\partial t}+\sigma_r \tilde{u}_2=-\bar{u}_r \tilde{\mathrm{v}}\\
&\frac{\partial \tilde{\mathrm{v}}_1}{\partial t}+\sigma_x \tilde{\mathrm{v}}_1=-\bar{u}\frac{\partial \tilde{\mathrm{v}}}{\partial x}\\
&\frac{\partial \tilde{\mathrm{v}}_2}{\partial t}+\sigma_r \tilde{\mathrm{v}}_2=-\frac{\partial \tilde{p}}{\partial r}\\
&\frac{\partial \tilde{\mathrm{w}}_1}{\partial t}+\sigma_x \tilde{\mathrm{w}}_1=-\bar{u}\frac{\partial \tilde{\mathrm{w}}}{\partial x}\\
&\frac{\partial \tilde{\mathrm{w}}_2}{\partial t}+\sigma_r \tilde{\mathrm{w}}_2=-\frac{im}{r}\tilde{p}\\
&\frac{\partial \tilde{p}_1}{\partial t}+\sigma_x \tilde{p}_1=-\bar{u}\frac{\partial \tilde{p}}{\partial x}-\frac{\partial \tilde{u}}{\partial x}\\
&\frac{\partial \tilde{p}_2}{\partial t}+\sigma_r \tilde{p}_2=-\frac{\tilde{\mathrm{v}}}{r}-\frac{\partial \tilde{\mathrm{v}}}{\partial r}-\frac{im}{r}\tilde{\mathrm{w}}
\end{aligned}
\tag{6}
$$

where $\tilde{u}=\tilde{u}_1+\tilde{u}_2$, $\tilde{\mathrm{v}}=\tilde{\mathrm{v}}_1+\tilde{\mathrm{v}}_2$, $\tilde{\mathrm{w}}=\tilde{\mathrm{w}}_1+\tilde{\mathrm{w}}_2$ and $\tilde{p}=\tilde{p}_1+\tilde{p}_2$. The absorption coefficients σ_x and σ_r are varied gradually in the PML domain. As shown in Fig.(3a) and Fig.(8a) the PML domains used for the open and the ducted rotor case, σ_x is set zero at the right and left PML domains and σ_r is zero at the top PML domain. At the corner regions, both coefficients are nonzero. In the present paper, the following form has been used for the variation of σ_x or σ_r within the PML domains:

$$\sigma=\sigma_{\max}(1.0-e^{-(d/D)^2}) \tag{7}$$

in which D is the width of the PML domain, d is the distance from its interface with the interior domain and $\sigma_{\max}$ is the maximum value of σ, which is dependent on grid size.

2.2 Solid Wall Boundary Condition

For the ducted rotor, on the surface of the duct wall, the fundamental physical requirement is the non-penetration boundary condition:

$$\vec{\mathrm{v}}\bullet\vec{n}=0 \;\; or \;\; \tilde{u}n_x+\tilde{\mathrm{v}}n_r+\tilde{\mathrm{w}}n_\theta=0 \tag{8}$$

where $\vec{n}$ is the unit normal on the wall and can be written as $\vec{n}=(n_x,n_r,n_\theta)=(0,\ 1,\ 0)$ for a plane wall. Then Eq.(8) becomes

$$\tilde{\mathrm{v}}=0 \tag{9}$$

By taking the dot product of the momentum equations of Eq.(5) with $\vec{n}$ for the plane wall, the Eq.(8) is equivalent to :

$$\frac{\partial \tilde{p}}{\partial r}=0 \tag{10}$$

In the case of the ducted rotor, both Eq.(9) and (10) are used on the wall surface. For the flat wall, Eq.(9) can be easily implemented. To satisfy Eq.(10), the numerical treatment in conjunction with high-order finite difference schemes derived by Tam and Dong [9] is implemented. In this method, ghost values of pressure are chosen so that Eq.(10) can be satisfied on each boundary condition enforcement point.

2.2 Conditions at the Centerline $r = 0$

As $r \to 0$, Eq.(5) has a numerical singularity and cannot be used directly. Since for $m \neq 0$ on the centerline $r = 0$, $\tilde{v} = \tilde{w} = \tilde{p} = 0$, the singularity terms in Eq.(5) may be replaced by partial derivative terms using L'Hospital's Rule, which are

$$\frac{\tilde{v}}{r} = \frac{\partial \tilde{v}}{\partial r}, \quad \frac{\tilde{w}}{r} = \frac{\partial \tilde{w}}{\partial r}, \quad \frac{\tilde{p}}{r} = \frac{\partial \tilde{p}}{\partial r} \tag{11}$$

at $r = 0$.

3. Multi-Domain Grid Design

Because of the disparity between the length scales in the source region and the acoustic wavelengths, a multi-domain Cartesian grid system is used. The computation domain is divided into several sub-domains enclosed by rectangular solid lines as shown in Fig.(2a) for an open rotor computation. For clarity, only part of the outside domain is given in Fig.(2a). The highest resolution is used in the area closest to the rotor blade or the source region respectively. When moving away from source region to the acoustic field, the grid size is stepped up by factors of two from inner to outer sub-domains. In principle, an overlapping grid technique for the use of high resolution schemes [11] can be used in the interface area. To make the computation more efficient, a special interface treatment between Cartesian grids was used. Since the grid spacing in adjacent Cartesian areas differs by a factor of 2, it is not difficult to form a 7 points DRP stencil at every point in region A with mesh size Δx or Δr and every point in region B (mesh size $\Delta x/2$ or $\Delta r/2$) except for points in the interface region, which is within a distance of three points from the interface in region B as shown in Fig.(2b). In the interface region, when grid lines on two grids coincide with each other, a cell-centered symmetric stencil with optimized coefficients is used, such as the point marked 'cc' in Fig.(2b). The stencil used at 'cc' can be written in the form

$$\left(\frac{\partial f}{\partial x}\right)_{cc} = \frac{1}{\Delta x}\sum_{j=-3}^{3} a_j f_j \tag{12}$$

The optimized stencil coefficients are

$$a_{-3} = -a_3 = -0.0046875$$
$$a_{-2} = -a_2 = 0.0651041666667$$
$$a_{-1} = -a_1 = -1.171875, \quad a_0 = 0.0$$

For the points on the non-coincidence lines, function values on several 'hanging' points marked as 'h' in Fig.(2b) are required. The values on these 'hanging' points are explicitly obtained by a two dimensional Lagrange interpolation. The interface treatments used here have been validated in ref.[6,7] on the basis of CAA Benchmark problems.

4. Artificial Selective Damping (ASD)

The ASD terms are added in the right hand side of the discretized finite difference equations in order to eliminate spurious short waves and improve numerical stability. In the interface regions among Cartesian grids, the irregularities are created by using different grid size and stencil. These irregularities are also very efficient in generating short spurious numerical waves. For the field points where the cell-centered

symmetric stencil Eq.(12) is used, a damping stencil with the same configurations was derived. The optimized stencil coefficients of the damping operator are

$$d_{-3} = d_3 = -0.01092915, \quad d_{-2} = d_2 = 0.06004774$$
$$d_{-1} = d_1 = -0.2991186, \quad d_0 = 0.5$$

In addition, for the grid points located at the centerline $r = 0$, the imposition of stronger ASD is required since there is a change of governing equations which may result in the generation of spurious short waves.

5. Numerical Simulations and Discussions

Numerical results on noise radiation from the open and ducted rotor will be discussed in the following sections. Because the variables $(\tilde{u}, \tilde{v}, \tilde{w}, \tilde{p})$ used in the governing equations are complex, the results presented are taken from Eq.(4) for zero azimuth angle $\theta = 0$. The directivity, $D(\phi)$, of the radiated sound is defined as

$$D(\phi) = R^2 \overline{p'^2(R, \phi, \theta, t)} \tag{13}$$

Where $\overline{\quad}$ is the time average. The definition of R and ϕ is given in Fig.(1) for the open rotor. For the ducted rotor, R is measured from the open end of the duct.

5.1 Open Rotor

The sound generated by an open rotor is simulated. Following body force distributions $(\tilde{F}_x, \tilde{F}_\theta)$ are used to simulate the impact of the rotor blades on the surrounding air[4].

$$\tilde{F}_\theta(x,r) = \begin{cases} F(x) r J_m(\alpha_{mN} r) & r \le 1 \\ 0 & r > 1 \end{cases}$$
$$\tilde{F}_x(x,r) = \begin{cases} F(x) J_m(\alpha_{mN} r) & r \le 1 \\ 0 & r > 1 \end{cases} \tag{14}$$
$$F(x) = \exp\left\{-(\ln 2)(x/h_w)^2\right\}, \quad h_w = 0.1$$

where $J_m(\ )$ is the m th-order Bessel function, α_{mN} is the Nth root of $J'_m(\alpha_{mN}) = 0$ and h_w is the half-width of the Gaussion-like forcing function. For a B blade rotor, the body force is spaced in $\frac{2\pi}{B}$ radians apart and spins with rotor rotational speed Ω. The m is chosen as the number of the rotor blades B. The choice of the Bessel functions in Eq.(14) has no other significance than making the analytical solution simple. The 8-blade rotor ($B = 8$) is involved in the computation. α_{mN} is chosen as $\alpha_{8,1} = 9.64742$ in which $N = 1$ so that the force in the radial direction corresponds to a mono-peak function. In ducted rotor, N has the meaning of the radial mode number.

The whole computational domain is $x \times r = [-17,\ 17] \times [0,\ 17]$. The problem is symmetric about the x-axis. Thus only the solution in the upper half $x - r$ plane needs to be computed. The symmetric condition is applied for $(\tilde{u}, \tilde{w}, \tilde{p})$ and the anti-symmetric condition is applied for $\tilde{v}$. The choice of the grid size depends on the acoustic wave length and h_w. In general, 4 grid points are necessary to resolve the half-width of the forcing function and the minimum of 8 grid points per wave length has to be used in the far-field.

Two rotational speeds are used, one with subsonic tip speed $\Omega = 0.85$ and the other with supersonic tip speed $\Omega = 1.15$. The grid sizes of the smallest domain are $\Delta x_s = 0.025$ for $\Omega = 0.85$ and $\Delta x_s = 0.02$ for $\Omega = 1.15$ respectively. The time advancing scheme used throughout the paper is the classical 4 stage Runge-Kutta scheme with a time step $\Delta t = 0.005$ if there is no other specification. In the open rotor computation, the mean flow $\bar{u}(r) = 0$ is assumed. The width of the PML domain is chosen as to contain 10 grid points.

Fig.(3) shows a snapshot of the acoustic pressure contours and the details of the multi-domain grid system for the open rotor with subsonic tip speed. The rectangular box in the plots is the interface between two Cartesian domains. The results show most of the acoustic radiation is concentrated in the direction around the plane of rotation. The results in zoom scale in Fig.(3b) also demonstrate that the contour lines go through grid interfaces very smoothly without any noticeable reflection. Fig.(4) gives the directivity at $R = 15.0$ obtained computationally in comparison with the exact solution [4] for $\Omega = 0.85$. There is good agreement between the numerical simulation and the analytical solution although the latter was obtained with the assumption of $R \to \infty$. To compare the effect of different far-field boundary conditions, the result with Tam's asymptotic far-field boundary condition is also presented in the figure. Only little difference was found. In addition, the comparison on the directivity for different rotational speed in Fig.(5) shows that, as expected, the radiation from the rotor with the supersonic tip speed is stronger.

5.2 Ducted Rotor

For the ducted rotor, the governing equations Eq.(5) are again used together with solid wall boundary conditions on both sides of the duct wall. In general, the effect of the duct wall will force the acoustic disturbance to be continuously reflected back and thereby cause cancellations and reinforcements. From the standard modal analysis of duct acoustic theory, the in-duct pressure for a cylinder duct can be expressed as superposition of various rotational modes,

$$p(r,\theta,x,t) = \sum_m \sum_{N=0}^{\infty} A_{mN} J_m(K_{mN} r) \exp[im(\theta - \Omega_m t) + iK_x x] \tag{15}$$

where m and N are the circumferential and the radial mode numbers respectively. In general, K_{mN} is called the radial wave number and can be obtained by satisfying the wall boundary condition. For a hard walled duct, K_{mN} is the N th root of $J'_m(K_{mN}) = 0$. Ω_m is the rotational speed of the m 's mode. When the body force felt by the B-blade rotor is steady (as in the present paper), the rotational speed of all modes is equal to Ω and the circumferential mode number m can only be chosen as $m = \mu B$, ($\mu = 1,2,3,\ldots$), therefore only the acoustic signal with frequency $f_\mu = \frac{\mu B \Omega}{2\pi} = \mu f_1$, is generated. f_1 is called rotor blade passing frequency (BPF).

From Eq.(15) it is known that whether an acoustic mode can be propagated along the duct (x) or not depends on the axial wave number K_x. For cylindrical ducts with uniform mean flow at a Mach number $M = \bar{u}$, K_x is obtained by

$$K_x = \frac{-KM + \sqrt{K^2 - K^2{}_{mN}(1 - M^2)}}{1 - M^2} \tag{16}$$

where $K = \mu B \Omega$ is the non-dimensional wave number of the acoustic disturbance. The modes with real K_x are the propagating modes and called cut-on modes. The modes with non-zero imaginary part of K_x are exponentially decaying in amplitude along the duct and therefore called cut-off modes.

From Eq.(16), it can be derived that the acoustic wave with BPF and its high harmonics f_μ can be propagated through the duct only if the rotational speed Ω satisfies,

$$\Omega > \frac{K_{mN}}{m}\sqrt{1-M^2} \tag{17}$$

where the right hand side of Eq.(17) is called cut-off rotational speed Ω_c in the present paper.

For the ducted rotor with the same body force function as Eq.(14) , the Eq.(15) can be simplified since the given body force function can only excite one rotational mode,

$$p(r,\theta,x,t) = J_m(K_{mN}r)\exp[im(\theta-\Omega t)+iK_x x] \tag{18}$$

where $K_{mN} = \alpha_{mN}$ and $m = B$ as well as $N = 1$ as specified.

5.2.1 Effect of Uniform Mean Flow on Noise Radiation from Open End of Duct

In the ducted rotor case, the same body force function Eq.(14) as for the open rotor is used. An infinitely thin duct wall is placed at $r = 1.0$ along $-4.1 \le x \le 8.0$. PML conditions are implemented on the left side of the duct to simulate an infinite length of the duct. Symmetry about the x-axis is assumed. The size of the computational domain is $[-4.1,\ 16.5]\times[0,\ 8]$.

For the case without considering any mean flow or $M = 0$, Ω_c is equal to 1.206 according to Eq.(17) when setting $m = B = 8$, $N = 1$, and $K_{mN} = \alpha_{mN} = \alpha_{8,1} = 9.64742$ as in the open rotor case. The two rotational speeds Ω used in the open rotor case are all smaller than $\Omega_c = 1.206$ so that all the acoustic disturbances are cut-off or evanescent. This can be seen as well by looking at the time history outside the duct. Fig.(6) gives the pressure time history sensed at $R = 6.0$ and $\phi = 52^\circ$ for $\Omega = 1.15$. R is measured from the center of the duct end located at $(x,r) = (8.0,\ 0.0)$. It shows that the intensity of sound radiation decreases very quickly after the initial transient state. Thus there is no sound radiation out of the open end of the duct even for slightly supersonic tip Mach number. This also proves that the environment around an acoustic source plays an important role in noise propagation.

From Eq.(17), it can be seen that, Ω_c will be reduced if mean flow is involved. Therefore, with changing the mean flow Mach number, the condition for Ω to either represent a propagational or non-propagational signal will also be changed. For example, for the case $M = 0.5$ inside and outside of the duct, Ω_c reduces to 1.044 so that the noise generated by the rotor with $\Omega = 1.15$ will radiate from the open end of the duct. The pressure time history for the ducted rotor with $\Omega = 1.15$ under uniform mean flow $M = 0.5$ is given in Fig.(7) at the same position as in Fig.(6). The results indicate that a time periodic state has been reached after the initial transient state due to sound radiation from the duct end. Fig.(8) shows the pressure contour at $t = 40$ and its enlarged plot close to the grid interface. The results prove again the numerical treatment is successful. It should be mentioned that since the pressure disturbance propagates in the duct on a helical path, the pressure contour given in Fig.(8) is only a cut in the three dimensional spiral pattern. Due to the mean flow convection effect, the spinning mode will propagate much faster in downstream direction of the rotor than upstream of the rotor. The difference of the length scale upstream and downstream of the rotor, as shown in Fig.(8) demonstrates the mean flow convection effect.

5.2.2 Effect of Shear Layer on Noise Radiation

In previous section, it was demonstrated that the effect of a mean flow in the duct may cause the propagation of acoustic modes which are cut-off for vanishing mean flow. Furthermore, when there are gradients in the mean flow typically due to the shear layer between the ambient medium and the jet flow

emanating from the duct, instability waves may be generated by acoustic excitation. Finally, the propagation of the acoustic waves through the shear layer will change the acoustic directivity pattern.

In order to show the main effect of the presence of such a shear layer an analytical shear flow was introduced separating the flow field in $r \le 1$ from the ambient medium. The parallel mean velocity profile is,

$$\overline{u}(r) = \begin{cases} M_\infty + (M - M_\infty)\exp\left\{-(\ln 2)\left(\frac{r-b}{h_w}\right)^2\right\} & r > b \\ M & h \ge r \ge 0 \end{cases} \tag{16}$$

where the mean flow is uniform inside $r \le 1$ with $M = 0.5$. The Gaussian distributed function is used to describe the variation of the shear flow. The half width of this function is $h_w = 0.25$. The other parameters are $b = 1.0$ and $M_\infty = 0.0$. The computation domain as well as the grid arrangement is the same as in Fig.(8). PML equations of Eq.(6) are again used. It should be mentioned that the shear layer chosen here is for the purpose of demonstrating the effect of the shear layer on noise propagation and not to show the excitation of the instability wave. No instability mode is indeed excited under the considered signal frequency.

Fig.(9) shows the instant pressure contour at two different times. Apart from the acoustic waves radiated from open duct end, depicted in Fig.(9a) a hydro-dynamical instability in form of a wave packet is observed inside the shear layer. The instability is convected out of the computation domain at later times as shown in Fig.(9b). Therefore these instability waves are believed to be excited purely by the multi-frequency transients occurring when the force Eq.(14) is turned on at $t = 0$. This demonstrates that the considered shear flow is stable for the acoustic excitation from the open duct end at $\Omega = 1.15$. The comparison of the directivity at $R = 6.0$ for uniform and shear layer mean flow is given in Fig.(10) which shows that the radiation pattern has been shifted upstream after passing through the shear layer.

6. Summary

The noise radiation from an open and ducted rotor is simulated using a CAA multi-domain method. The results for the ducted rotor show that there is no sound radiation out of the open end of the duct when the rotational speed of the ducted rotor is below the cut-off rotational speed. The sound field generated by an open and ducted rotor can be extremely different because the presence of the duct wall will cause cancellations and reinforcements of both propagating and reflecting waves. The effect of mean flow in the duct may cause the propagation of the acoustic modes which are cut-off for no flow. The validations using benchmark problems for the open rotor case also show that the presented method has good accuracy in terms of the schemes and the boundary conditions used.

7. Reference

1. Ffowcs Wiliams, J., Hawkings, D.: Sound Generation by Turbulence and Surfaces in Arbitrary Motion, Phil. Trans. Roy. Soc. A264, 1969.
2. Brentner, K. S.; Farassat, F.: Helicopter Noise Prediction: The Current Status and Future Direction, DGLR/AIAA 14th Aeroacoustics Conference, Aachen, Germany, 1992.
3. Tam, C.K.W.: Computation Aeroacoustics: Issues and Methods, AIAA J. Vol. 33, pp.1788-1796, Oct. 1995.
4. Third Computational Aeroacoustics (CAA) Workshop on Benchmark Problems, NASA CP 2000-209790, Edited by Milo, D. Dahl, August, 2000.
5. Hu, F. Q. : On Perfectly Matched Layer as An Absorbing Boundary Condition, AIAA 96-1664, 1996.
6. Delfs, J., Yin, J. "CAA-Simulation of Aeroacoustic Sources on Overlapped grids". Second Aeroacoustic Workshop SWING, Braunschweig (de), 06.-07.10.2000, DLR, (2000)

7. Yin, J. and Delfs, J.W. Sound Generation from Gust-Airfoil Interaction using CAA-Chimera Method. AIAA Paper 2001-2136, 7th AIAA/CEAS Aeroacoustics Conference 2001.
8. Tam, C.K.W. and Webb, J.C. "Dispersion Relation Preserving Finite Difference Schemes for Computational Acoustics", J. Comp. Phys.,107,262-281,1993.
9. Tam, C.K.W. and Dong, Z. "Wall Boundary Conditions for High-order Finite Difference Schemes in Computational Aeroacoustics", Theoretical and Computational Fluid Dynamics, 6, 303-322,1994.
10.Tam, C.K.W. and Dong, Z. "Radiation and Outflow Boundary Conditions for Direct Computation of Acoustic and Flow Disturbances in a Nonuniform Mean Flow", CEAS/AIAA Paper 95-007,June 1995.
11.Delfs, J. W. "An overlapping grid technique for the use of high resolution schemes of computational aeroacoustics at complex geometries". AIAA Paper 2001-2199, 7th AIAA/CEAS Aeroacoustics Conference 2001.

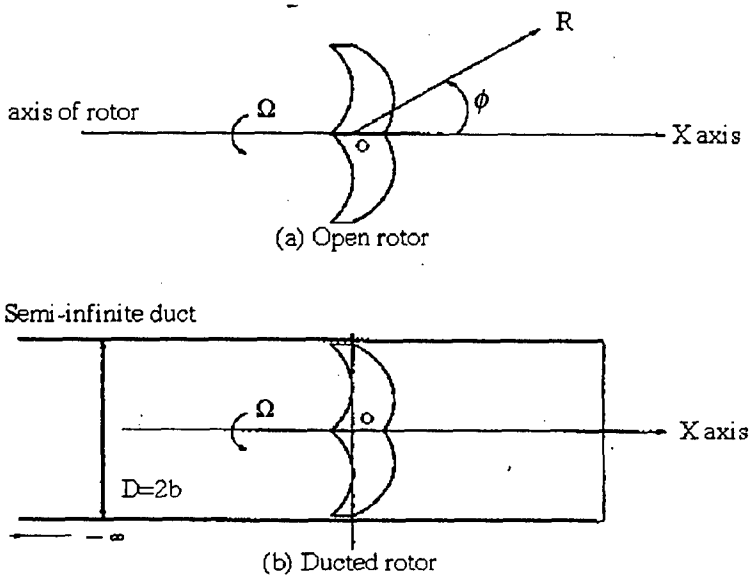

Fig. 1 A sketch of the open and ducted rotor problems

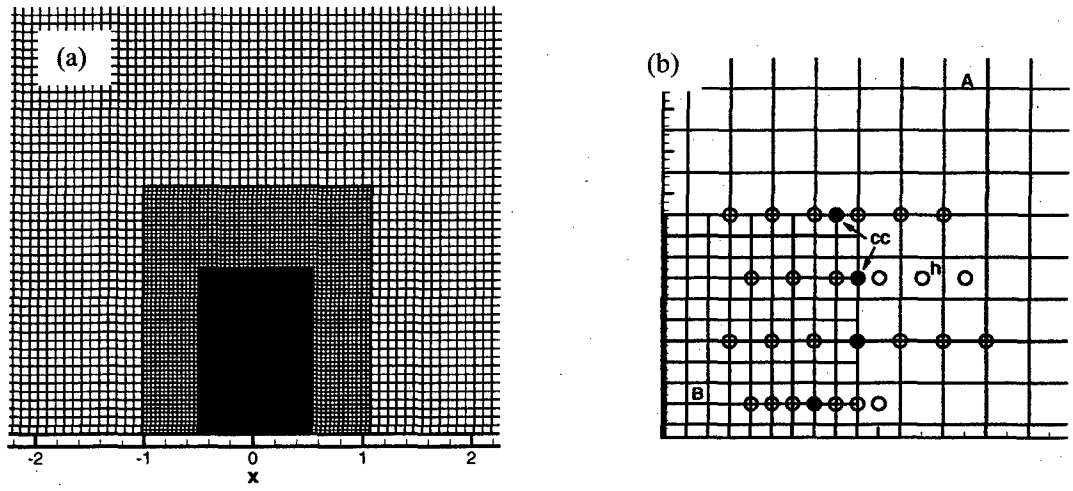

Fig. 2 (a) Multi-domain grid system used for the open rotor computation
(b) Special interface treatment between Cartesian grids

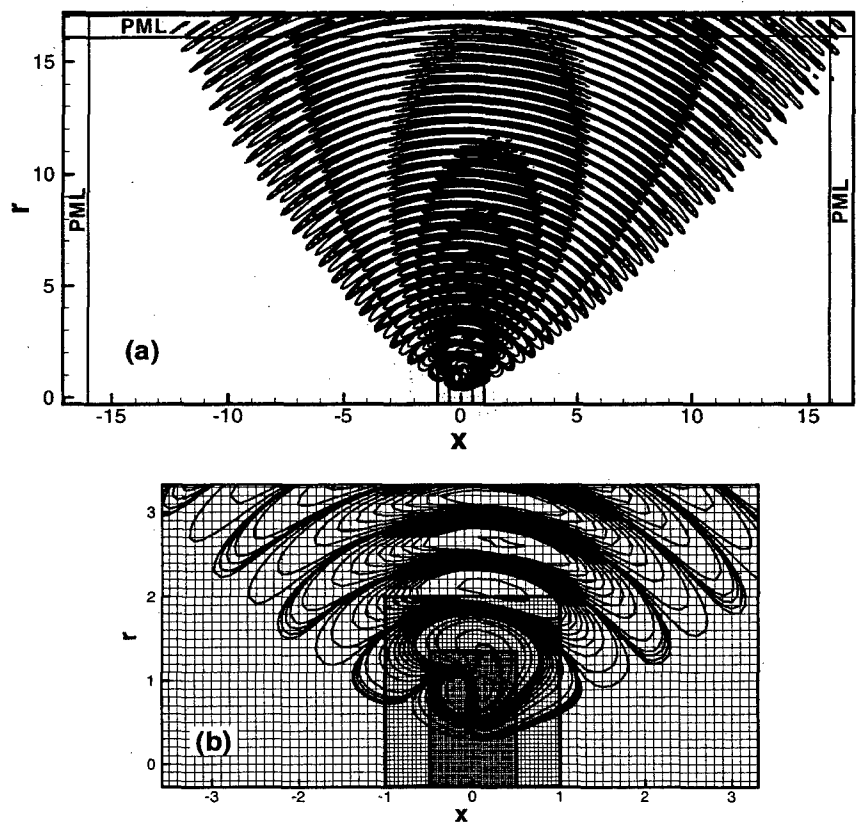

Fig. 3 (a) Acoustic pressure contour for the open rotor with $\Omega = 0.85$
(b) A zoom view from (a) in the area close to the rotor

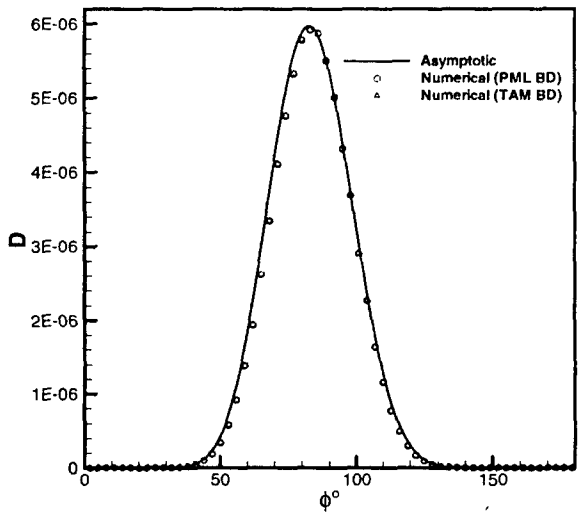

Fig. 4 Comparison of the numerically obtained directivity at $R = 15.0$ and the exact solution [4] for $\Omega = 0.85$ with two different far-field (PML and TAM) boundary conditions (BD)

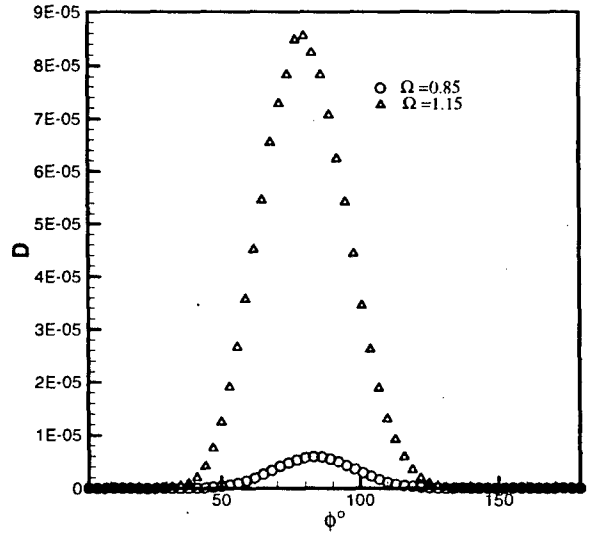

Fig. 5 Comparison of the directivity for different rotational speeds

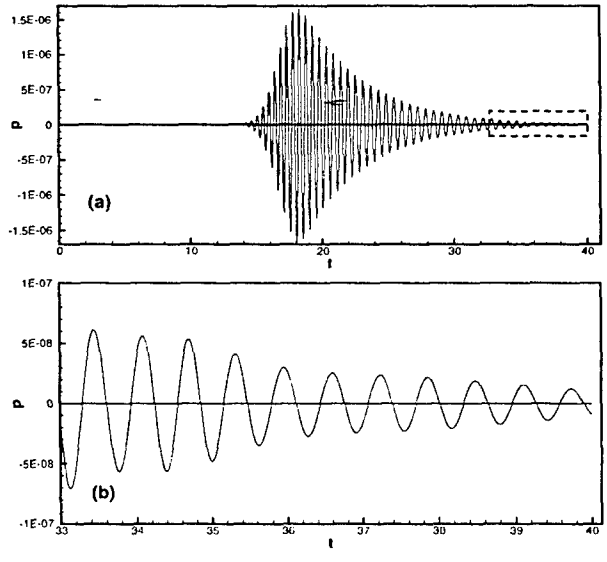

Fig. 6 (a) Pressure time history sensed at $R = 6.0$ and $\Phi = 52^{\circ}$ for $\Omega = 1.15$ (b) Zoom-view of the box in (a); ducted rotor case with M = 0.0.

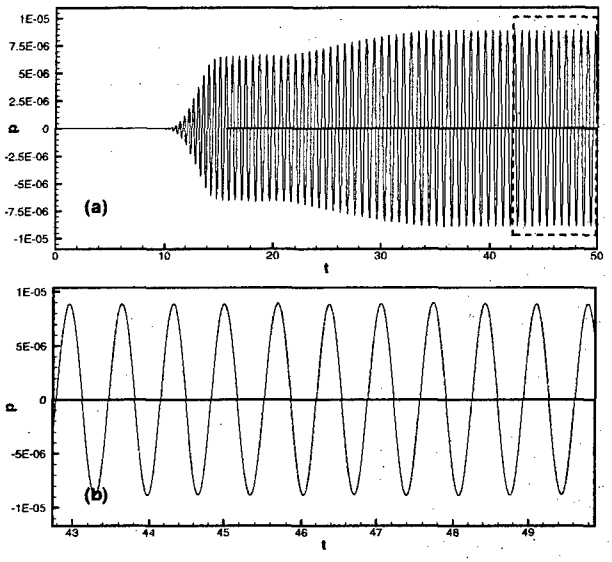

Fig. 7 (a) Pressure time history sensed at $r = 6.0$ and $\Phi = 52^{\circ}$ for $\Omega = 1.15$ (b) Zoom-view of the box in (a); ducted rotor case with M = 0.5.

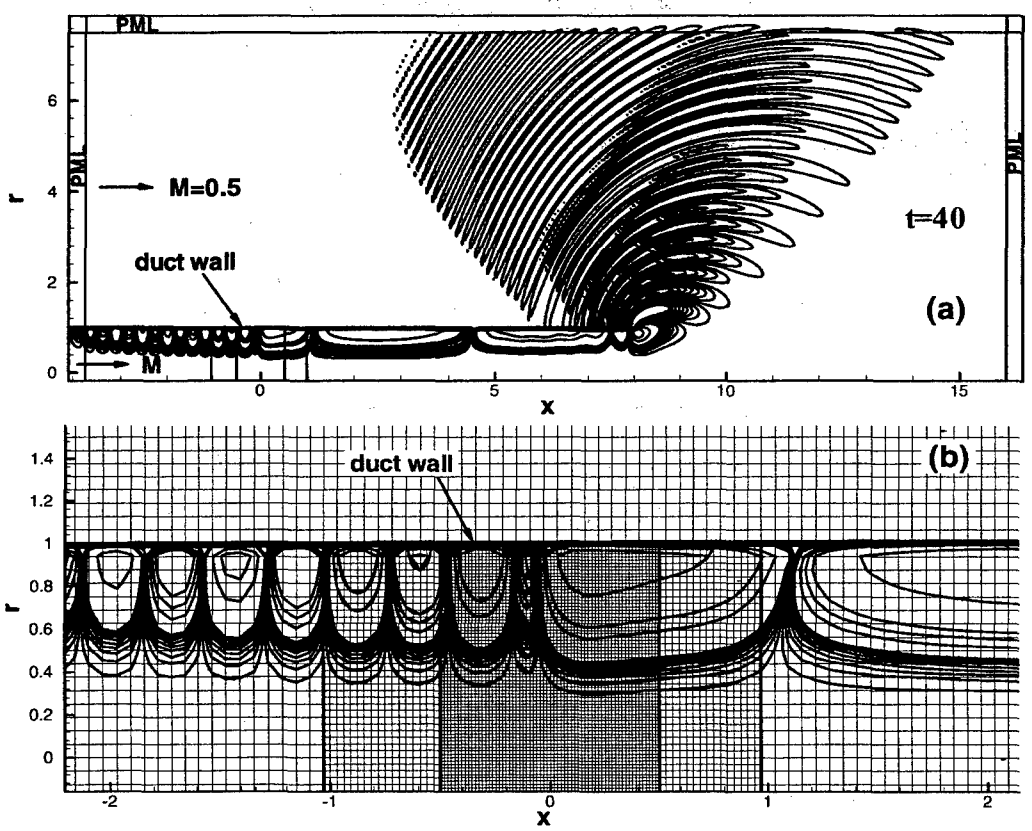

Fig. 8 Pressure contour at $t = 40.$ and its enlarged plot close to grid interface; ducted rotor case with M = 0.5 and $\Omega = 1.15$

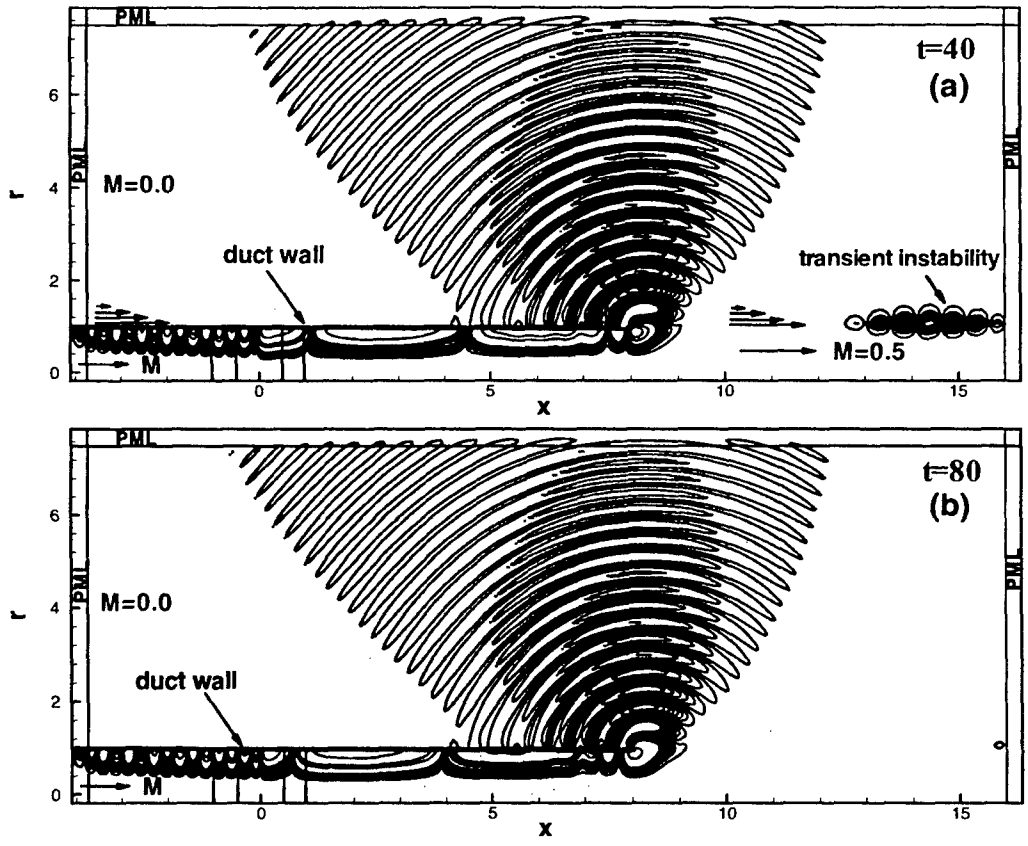

Fig. 9 Pressure contour at two different times; ducted rotor case with a given shear flow and $\Omega = 1.15$

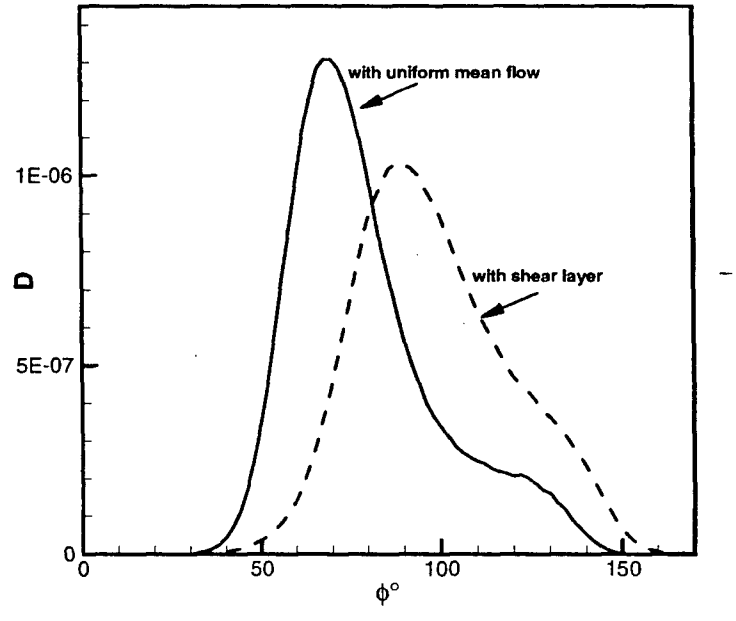

Fig. 10 Comparison of noise radiation directivity at $R = 6.0$ for uniform mean flow and mean flow with shear layer

Reference # of Paper: 2
Discusser's Name: Mr. Jose M. Riola Rodriguez
Author's Name: Dr. Jianping Yin
Question:

Do you think this model is applicable to swirling flows or only in axial flows?

Answer:

Yes. The method itself is not limited to axial flows.

Discusser's Name: Dr. Brian J. Tester
Author's Name: Dr. Yianping Yin
Question:

Is the free shear layer of the jet being modeled as well as the shear layer on the outside of the duct?

Answer:

No. The shear layer separating the jet and the ambient medium is modeled by an analytical, parallel flow profile. This profile is only imposed on the outside of the duct wall.